Above-threshold ionization of helium in the long-wavelength regime: Examining the single-active-electron approximation and the two-electron strong-field approximation

Chuan Yu and Lars Bojer Madsen

Department of Physics and Astronomy, Aarhus University, DK-8000 Aarhus C, Denmark

We investigate high-order above-threshold ionization of model helium in the long-wavelength regime up to 2400 nm by solving the two-electron time-dependent Schrödinger equation in one dimension. To bypass the difficulty of solving the multielectron time-dependent Schrödinger equation with the long-wavelength laser interaction, we revisit and examine two typically used theoretical methods: the single-active-electron approximation and the strong-field approximation. For the description of the high-energy rescattered electrons in the ground-state ionic channel, the single-active-electron approximation performs better with increasing ponderomotive energy. Single ionization in the excited-state ionic channels, in general, has much weaker spectral intensity than that in the ground-state ionic channel. The above-threshold-ionization cutoffs in the excited-state ionic channels are clear signatures of two-electron dynamics, which cannot be explained within the single-active-electron approximation. By applying the two-electron strong-field approximation including rescattering and a saddle-point method analysis, we explain the channel-resolved cutoffs, and relate them to elastic and inelastic rescattering processes.

I. INTRODUCTION

Above-threshold ionization (ATI) of atoms and molecules, in which more photons than the minimum required for ionization are absorbed from the laser field, is one of the most fundamental phenomena in strong-field physics. Since the first experimental observation of ATI [1], numerous studies have been performed to explore the ATI spectral features (see, e.g., Refs. [2–4] for reviews). When irradiated by an intense laser field, a bound electron may be freed, drift away, and contribute to the low-energy part of the ATI spectrum (typically below $2U_p$, where U_p is the ponderomotive energy). Alternatively it may be driven back to the ion by the laser field and rescatter. The backscattered electrons gain more energy than the direct electrons and contribute to the plateau-like high-energy part of the ATI spectrum, typically ranging from $2U_p$ to $10U_p$. The high-energy region of the ATI spectrum is found to be particularly sensitive to the structure of the target ion, allowing for imaging applications. For example, laser-induced electron diffraction (LIED) [5] is a time-resolved molecular self-imaging technique based on extracting structural information from strong-field-induced rescattering.

Recent development of intense few-cycle light sources with long wavelengths, e.g., in the mid-infrared regime, opens a new avenue of strong-field physics [6]. With long-wavelength laser pulses used in the LIED, one can produce very high energy rescattered electrons for imaging ultrafast molecular dynamics, with femtosecond and subangstrom resolution [7–9]. Although strong-field ionization in the long-wavelength regime is promising in experimental research, the corresponding numerical simulations are very challenging. The difficulties of solving the time-dependent Schrödinger equation (TDSE) in the long-wavelength regime come not only from the involvement of many angular momentum states but also from the large quiver radius that is proportional to the wavelength squared. It is, hence, a formidable task to simulate multielectron dynamics in the long-wavelength regime. So a question arises: what theoretical methods other than full

TDSE calculations are useful for studying the long-wavelength laser interaction with multielectron systems? In this paper, we discuss this question by examining the single-active-electron approximation (SAEA) and the two-electron strong-field approximation (SFA) including rescattering. We focus on the high-energy part of the ATI spectrum, which can be used for high-resolution imaging with the LIED technique.

The SAEA assumes that only one electron is bound by an effective potential and interacts with the laser field. However, the validity of the SAEA in few-electron systems still remains not fully investigated. In the long-wavelength regime, it is particularly difficult to examine the validity of the SAEA, since *ab initio* calculations beyond the SAEA are extremely demanding. To overcome this difficulty, we consider a one-dimensional (1D) model of helium in the presence of linearly polarized infrared laser fields, and the maximum wavelength considered is 2400 nm. For such a long wavelength, single ionization (SI) is dominant. We compute the SI spectra in different ionic channels corresponding to different final states of He$^+$, and compare them with the ATI spectra obtained within the SAEA. In the long-wavelength regime, or the strong-field regime with large U_p, the SAEA is found to be applicable for describing the high-order ATI in the lowest ionic channel, which is the dominant SI channel. To some extent, this validates the commonly used single-active-electron model.

In the two-electron TDSE calculations, however, there also exist two-electron effects even in the SI channels, which cannot be described within the SAEA. The channel-resolved ATI spectra, especially those in the excited-state ionic channels, contain clear two-electron features. To investigate the two-electron features and the corresponding physical processes, one needs theoretical methods beyond the SAEA. The SFA, also known as the Keldysh-Faisal-Reiss theory [10–12], and its modified versions have been extensively applied to investigate both one-electron and two-electron dynamics (see, e.g., Refs. [13–25]). To our knowledge, the SFA has not been applied for the description of the channel-resolved high-order ATI spectra. In this paper, we formulate the two-electron

SFA including rescattering for the channel-resolved ATI of helium and apply the saddle-point method (SPM) to analyze the spectral cutoffs. As we will show, the SFA and the SPM enable us to qualitatively explain the channel-resolved ATI cutoffs, and to relate them to elastic and inelastic rescattering processes. In this sense the SFA is a useful tool for qualitative studies of the strong-field ionization in the long-wavelength regime and for gaining physical insight about the relevant processes.

This paper is organized as follows. In Sec. II, we introduce the theoretical models and numerical methods used in the TDSE calculations, and formulate the SAEA and the SFA for our model. In Sec. III we present and discuss the results of the calculations. Finally we give concluding remarks in Sec. IV. Atomic units are used throughout unless stated otherwise.

II. THEORETICAL MODELS AND METHODS

A. TDSE of the 1D helium model

We solve the TDSE of the widely used 1D two-electron model [26–28]

$$i\partial_t \Psi(x_1,x_2,t) = H(t)\Psi(x_1,x_2,t), \qquad (1)$$

with the Hamiltonian

$$H(t) = \sum_{j=1}^{2}\left\{\frac{[p_j + A(t)]^2}{2} + V_{\mathrm{en}}(x_j)\right\} + V_{\mathrm{ee}}(x_1,x_2). \quad (2)$$

Here x_j and $p_j = -i\partial_{x_j}$ ($j = 1,2$) are the electron coordinate and momentum operators, respectively;

$$V_{\mathrm{en}}(x_j) = \frac{-2}{\sqrt{x_j^2 + 1}}, \quad (j = 1,2), \qquad (3)$$

$$V_{\mathrm{ee}}(x_1,x_2) = \frac{1}{\sqrt{(x_1 - x_2)^2 + 1}} \qquad (4)$$

are the electron-nucleus and the electron-electron interactions, which are softened to avoid the Coulomb singularity. The laser interaction is described in velocity gauge by the vector potential $A(t)$ within the dipole approximation. In our calculations, a vector potential with the sine-squared envelope is used:

$$A(t) = \begin{cases} -\frac{F_0}{\omega}\sin^2\left(\frac{\omega t}{2N_c}\right)\cos(\omega t), & 0 < t < \frac{2\pi N_c}{\omega}, \\ 0, & \text{else,} \end{cases} \quad (5)$$

where F_0 is the maximum field strength related to the peak intensity I (in units of W/cm^2) by $F_0 = \sqrt{I/(3.509 \times 10^{16})}$, ω is the angular frequency, and N_c is the number of cycles. We consider $N_c = 2$ to shorten the simulation time. For a laser pulse with a wavelength of 2400 nm and a peak intensity of 8×10^{13} W/cm^2, the electron quiver radius is $\alpha_0 = F_0/\omega^2 \approx 132$, which is the largest quiver radius considered in this work.

When numerically solving the TDSE, we discretize the simulation volume by employing a finite-element discrete variable representation (FEDVR) [29] combined with infinite-range exterior complex scaling (irECS) [30]. The coordinate space is divided into inner and outer regions by a complex scaling radius r_c, which is chosen to be larger than the

quiver radius. For example, we choose $r_c = 150 > \alpha_0$ for the laser parameters $\lambda = 2400$ nm and $I = 8 \times 10^{13}$ W/cm^2. The inner region $[-r_c,r_c]$ is discretized by finite elements with a fixed equal size of 2 and 11 Gauss-Lobatto basis functions in each element. The outer regions $(-\infty, -r_c]$ and $[r_c, +\infty)$ are complex scaled with a scaling angle $\theta = 0.3$ and discretized by 100 basis functions (see Refs. [30,31] for details of the irECS method and the basis functions). The number of outer-region basis functions used in our work is larger than that used in Refs. [30,31], where the numerical calculations were performed for 800 nm only. For the long-wavelength regime (e.g., 1600 nm and 2400 nm), we find that more outer-region basis functions are needed for convergence than the typically ~ 40 needed for 800 nm calculations.

We propagate the TDSE with the Arnoldi-Lanczos time propagator [32,33] with a time step of $\Delta t = 0.001$. The initial wave function is obtained by imaginary-time propagation (ITP) [34]. For both the two-electron TDSE and the one-electron TDSE within the SAEA, we extract the ATI spectra (dP/dk, where k is the final momentum of the freed electron) by using the time-dependent surface flux (tSURFF) method [35–37] with the tSURFF surfaces placed at $x = \pm 55$. We emphasize that the irECS method works as an efficient absorber so that the wave function in the inner region remains accurate for applying the tSURFF method. For the TDSE within the SAEA, we perform reference calculations on a large grid without any absorber (a finite simulation box $[-10000,10000]$ discretized by 10000 equal-size finite elements and 11 Gauss-Lobatto basis functions in each element). The convergence of the irECS method for the SAEA calculations is checked by comparison with the reference results. We apply the one-electron irECS parameters found by this convergence test also for the two-electron TDSE.

B. SAEA for the 1D helium model

Here we briefly introduce the SAEA used in this work (see also Ref. [38]). To find the effective potential, we first make the Hartree-Fock (HF) ansatz for the ground-state He wave function and apply ITP to the equation for the field-free single-electron orbital ψ_0,

$$i\partial_t \psi_0(x,t) = H_0(t)\psi_0(x,t), \qquad (6)$$

with the Hamiltonian

$$H_0(t) = \frac{p^2}{2} + V_{\mathrm{en}}(x) + \int dx' V_{\mathrm{ee}}(x,x')|\psi_0(x',t)|^2. \quad (7)$$

The SAEA assumes that the inactive electron is "frozen" in the field-free single-electron orbital ψ_0 while the active electron feels the effective potential of the "frozen core"

$$V_{\mathrm{eff}}(x) = V_{\mathrm{en}}(x) + \int dx' V_{\mathrm{ee}}(x,x')|\psi_0(x')|^2, \qquad (8)$$

where the time dependence of ψ_0 is dropped since the distribution of the inactive electron $|\psi_0(x',t)|^2$ remains time-invariant. With the laser interaction taken into account, the TDSE for the active electron reads

$$i\partial_t \psi_1(x,t) = H_1(t)\psi_1(x,t), \qquad (9)$$

where the SAEA Hamiltonian is

$$H_1(t) = \frac{[p + A(t)]^2}{2} + V_{\text{eff}}(x). \tag{10}$$

The ionization potential (I_p) obtained within the SAEA is 0.750, which is slightly smaller than I_p for the SI of the two-electron model (0.755), due to the HF ansatz made in the SAEA.

C. Two-electron SFA for the 1D helium model

The way in which we formulate the two-electron SFA including rescattering follows the intense-field many-body S-matrix theory (IMST) [39], which is a systematic method to calculate the transition amplitude from an initial state $\psi_i(t_i)$ to a final state $\psi_f(t_f)$, based on different partitions of the total Hamiltonian. The states $\psi_i(t)$ and $\psi_f(t)$ are solutions to the TDSE with the Hamiltonians $H_i(t)$ and $H_f(t)$, respectively. We have the initial- and final-state partitions of the total Hamiltonian $H(t) = H_i(t) + V_i(t) = H_f(t) + V_f(t)$. Instead of using Green's functions as in Ref. [39], we formulate the theory with time-evolution operators $U(t,t')$, $U_i(t,t')$, and $U_f(t,t')$, corresponding to $H(t)$, $H_i(t)$, and $H_f(t)$, respectively. The time-evolution operators solve the TDSEs

$$i\partial_t U(t,t') = H(t)U(t,t'), \tag{11}$$

$$i\partial_t U_i(t,t') = H_i(t)U_i(t,t'), \tag{12}$$

$$i\partial_t U_f(t,t') = H_f(t)U_f(t,t'), \tag{13}$$

and the total time-evolution operator $U(t,t')$ can be related to $U_i(t,t')$ and $U_f(t,t')$ by

$$U(t,t') = U_i(t,t') - i\int_{t'}^{t} dt_1 U(t,t_1)V_i(t_1)U_i(t_1,t'), \tag{14}$$

$$U(t,t') = U_f(t,t') - i\int_{t'}^{t} dt_1 U_f(t,t_1)V_f(t_1)U(t_1,t'). \tag{15}$$

Substituting Eq. (15) into Eq. (14) leads to

$$U(t,t') = U_i(t,t') - i\int_{t'}^{t} dt_1 U_f(t,t_1)V_i(t_1)U_i(t_1,t')$$

$$- \int_{t'}^{t} dt_1 \int_{t_1}^{t} dt_2 U_f(t,t_2)V_f(t_2)U(t_2,t_1)$$

$$\times V_i(t_1)U_i(t_1,t'). \tag{16}$$

By evolving the system from $\psi_i(t_i)$ and applying Eq. (16), we can evaluate the probability amplitude of finding the system in $\psi_f(t_f)$ as

$$\langle \psi_f(t_f)| U(t_f,t_i) |\psi_i(t_i)\rangle$$

$$= \langle \psi_f(t_f)|\psi_i(t_f)\rangle - i\int_{t_i}^{t_f} dt_1 \langle \psi_f(t_1)| V_i(t_1) |\psi_i(t_1)\rangle$$

$$- \int_{t_i}^{t_f} dt_1 \int_{t_1}^{t_f} dt_2 \langle \psi_f(t_2)|V_f(t_2)U(t_2,t_1)V_i(t_1)|\psi_i(t_1)\rangle, \tag{17}$$

which is equivalent to the IMST expression [39].

In this work, the He ground state (denoted by $|g;t\rangle$ for time t) is considered as the initial state, so the initial-state partition of the total Hamiltonian is

$$H_i = \sum_{j=1}^{2}\left[\frac{p_j^2}{2} + V_{\text{en}}(x_j)\right] + V_{\text{ee}}(x_1,x_2), \tag{18}$$

$$V_i = A(t)[p_1 + p_2 + A(t)]. \tag{19}$$

For the channel-resolved SI, we consider the single-continuum state as the final state. In the SFA, exact continuum states are approximated by Volkov states, so we use the product of the Volkov state and the bound ionic state for the channel-specific single-continuum state. Reserving the index 1 for the freed electron, we have the final-state partition of the total Hamiltonian

$$H_f = \frac{[p_1 + A(t)]^2}{2} + \frac{p_2^2}{2} + V_{\text{en}}(x_2), \tag{20}$$

$$V_f = A(t)[p_2 + A(t)/2] + V_{\text{en}}(x_1) + V_{\text{ee}}(x_1,x_2). \tag{21}$$

Now we introduce the notation $|k,n;t\rangle$ for the approximated single-continuum state (the product of the Volkov state and the bound ionic state) at time t, meaning that the freed electron has the canonical momentum k and the ion He$^+$ is in its nth state. Thus the time-evolution operator $U_f(t,t')$ can be expressed as

$$U_f(t,t') = \sum_n \int_{-\infty}^{+\infty} dk \, |k,n;t\rangle \, \langle k,n;t'| . \tag{22}$$

By approximating $\langle k,n;t|g;t'\rangle \approx 0$ and $U(t_2,t_1) \approx U_f(t_2,t_1)$ in Eq. (17), we obtain the two-electron SFA transition amplitude from the initial state $|g;t = -\infty\rangle$ to the final state $|k_f,n;t = +\infty\rangle$:

$$T_{\text{SFA}}(k_f,n)$$

$$= -i\int_{-\infty}^{+\infty} dt_1 \langle k_f,n;t_1| V_i(t_1) |g;t_1\rangle$$

$$- \sum_m \int_{-\infty}^{+\infty} dt_1 \int_{t_1}^{+\infty} dt_2 \int_{-\infty}^{+\infty} dk_i \langle k_f,n;t_2| V_f(t_2) |k_i,m;t_2\rangle$$

$$\times \langle k_i,m;t_1| V_i(t_1) |g;t_1\rangle . \tag{23}$$

The spectral intensity is proportional to $|T_{\text{SFA}}(k_f,n)|^2$. For two-electron systems, the SFA has been extensively used in the studies of double ionization (see, e.g., Refs. [14,17,22–25]). In this work, we formulate the two-electron SFA [Eq. (23)] for the channel-resolved SI.

The physical meaning of Eq. (23) is clear: the first term describes the direct SI into the nth ionic channel via the laser interaction while the second term (sum) describes two-step processes leading to SI, including the rescattering. In the two-step processes, the first step, similar to the direct SI, is the SI (with intermediate momentum k_i) into the mth ionic channel induced by the laser interaction. The second step can be understood by investigating the three terms in Eq. (21): remember that the freed electron is denoted by the index 1, the first interaction $A(t_2)[p_2 + A(t_2)/2]$ can give a nonvanishing contribution only if $k_f = k_i$, describing a transition in the ion induced by the laser interaction; the second interaction $V_{\text{en}}(x_1)$ can give a nonvanishing contribution only if n and m are equal, describing an elastic rescattering of the freed electron via the

electron-nucleus interaction; the third interaction $V_{ee}(x_1,x_2)$ allows for state changes in both the freed and bound electrons, i.e., $k_i \to k_f$ and $m \to n$, including both elastic and inelastic rescattering processes via the electron-electron interaction.

Here we focus on the high-energy channel-resolved ATI cutoffs; therefore in the two-electron SFA we only study the terms that can contribute to the production of high-energy electrons, i.e., the terms corresponding to rescattering processes. For the high-energy part of the ATI spectra, Eq. (23) can be approximated by a sum of all the rescattering terms that result in the same final state $|k_f, n; t = +\infty\rangle$:

$$T_{\text{SFA}}(k_f, n) \approx \sum_m T_{\text{res}}^{m,n}(k_f), \qquad (24)$$

where $T_{\text{res}}^{m,n}(k_f)$ is a unified notation for both the elastic ($m = n$) and inelastic ($m \neq n$) rescattering terms:

$$T_{\text{res}}^{m,n}(k_f) = -\int_{-\infty}^{+\infty} dt_1 \int_{t_1}^{+\infty} dt_2 \int_{-\infty}^{+\infty} dk_i \, \langle k_f, n; t_2 | V_{\text{res}} | k_i, m; t_2\rangle$$
$$\times \, \langle k_i, m; t_1 | V_i(t_1) | g; t_1\rangle . \qquad (25)$$

In Eq. (25) the notation V_{res} is used for both the elastic ($m = n$) and inelastic ($m \neq n$) rescattering interactions, which are time-independent:

$$V_{\text{res}}^{m,n} = \delta_{m,n} V_{en}(x_1) + V_{ee}(x_1,x_2). \qquad (26)$$

With the He ground-state energy denoted by E_g and the nth (mth) ionic energy denoted by E_n (E_m), we introduce the two-electron Volkov phase

$$S_{k_f}^{m,n}(k_i, t_1, t_2) = \int_0^{t_2} dt \frac{[k_f + A(t)]^2}{2} - \int_{t_1}^{t_2} dt \frac{[k_i + A(t)]^2}{2}$$
$$+ (E_n - E_m)t_2 + (E_m - E_g)t_1, \qquad (27)$$

and the form factor

$$W_{k_f}^{m,n}(k_i, t_1) = \langle k_f, n; 0| V_{\text{res}}^{m,n} | k_i, m; 0\rangle$$
$$\times \, \langle k_i, m; 0| V_i(t_1) | g; 0\rangle . \qquad (28)$$

Then Eq. (25) can be rewritten as

$$T_{\text{res}}^{m,n}(k_f) = - \int_{-\infty}^{+\infty} dt_1 \int_{t_1}^{+\infty} dt_2 \int_{-\infty}^{+\infty} dk_i \big\{ W_{k_f}^{m,n}(k_i, t_1)$$
$$\times \, \exp\big[i S_{k_f}^{m,n}(k_i, t_1, t_2)\big]\big\}. \qquad (29)$$

The SPM is applied to approximate the integral in Eq. (29) (see, e.g., Refs. [13,15,19] for discussion of the SFA and the SPM). First, we seek for solutions to the saddle-point equations

$$\frac{\partial S_{k_f}^{m,n}}{\partial k_i} = \frac{\partial S_{k_f}^{m,n}}{\partial t_1} = \frac{\partial S_{k_f}^{m,n}}{\partial t_2} = 0, \qquad (30)$$

namely,

$$k_i(t_2 - t_1) + \int_{t_1}^{t_2} dt \, A(t) = 0, \qquad (31)$$

$$\frac{[k_i + A(t_1)]^2}{2} + (E_m - E_g) = 0, \qquad (32)$$

$$\frac{[k_f + A(t_2)]^2}{2} - \frac{[k_i + A(t_2)]^2}{2} + (E_n - E_m) = 0. \qquad (33)$$

Equation (31) determines the intermediate momentum k_i while Eqs. (32) and (33) describe the energy conservation at the

ionization time t_1 and the rescattering time t_2. The solutions are complex-valued and they come in pairs. We only consider the physically relevant solutions, with additional conditions $0 < \text{Re}(t_1) < \text{Re}(t_2) < 2\pi N_c/\omega$ and $\text{Im}(t_1) > 0$ imposed. The nonlinear Eqs. (31)–(33) are solved numerically with the Powell hybrid method.

Suppose that there are Q pairs of physically relevant solutions for any final momentum k_f. We introduce an index $s \in \{q+, q-\}$ ($q = 1, \ldots, Q$) for the solutions $\{k_i^s, t_1^s, t_2^s\}$, and approximate Eq. (29) according to the SPM

$$T_{\text{res}}^{m,n}(k_f) \sim - \sum_s \big\{ W_{k_f}^{m,n}(k_i^s, t_1^s) \exp\big[i S_{k_f}^{m,n}(k_i^s, t_1^s, t_2^s)\big]$$
$$\times \big[\Delta_{k_f}^{m,n}(k_i^s, t_1^s, t_2^s)\big]^{-1/2}(2\pi i)^{3/2}\big\}, \qquad (34)$$

where $\{k_i^s, t_1^s, t_2^s\}$ are the solutions to Eqs. (31)–(33) and

$$\Delta_{k_f}^{m,n}(k_i, t_1, t_2) = \frac{\partial^2 S_{k_f}^{m,n}}{\partial k_i^2} \frac{\partial^2 S_{k_f}^{m,n}}{\partial t_1^2} \frac{\partial^2 S_{k_f}^{m,n}}{\partial t_2^2}. \qquad (35)$$

The ATI cutoff energy is solely determined by the exponential term within the SPM. The SPM fails for electron energies near and beyond the cutoff; i.e., the pair of two solutions approach each other closely near the cutoff and one of them becomes unphysical after the cutoff. The contribution of the unphysical solution diverges as the energy $k_f^2/2 \to +\infty$ (see, e.g, Refs. [13,15,18]). To solve this problem, one can drop the unphysical solution for energies beyond the cutoff, or use the uniform approximation [15,19]. For a pair of solutions $\{k_i^{q+}, t_1^{q+}, t_2^{q+}\}$ and $\{k_i^{q-}, t_1^{q-}, t_2^{q-}\}$ as a function of the final momentum k_f, a cutoff energy $k_f^2/2$ can be determined by finding the k_f that satisfies the condition

$$\text{Re}\big[S_{k_f}^{m,n}(k_i^{q+}, t_1^{q+}, t_2^{q+})\big] = \text{Re}\big[S_{k_f}^{m,n}(k_i^{q-}, t_1^{q-}, t_2^{q-})\big]. \qquad (36)$$

Here we reserve the index $\{q-\}$ for the unphysical solution after the cutoff. There might be multiple pairs of solutions that give different cutoff energies; however, the observed or numerically obtained ATI cutoff is typically determined by only one pair of solutions. In this work we apply the SFA and the SPM to investigate the channel-resolved ATI cutoffs, and we neglect the form factor $W_{k_f}^{m,n}(k_i^s, t_1^s)$ in Eq. (34), which does not affect the cutoffs. Denoting by $\{k_i^{c+}, t_1^{c+}, t_2^{c+}\}$ and $\{k_i^{c-}, t_1^{c-}, t_2^{c-}\}$ the dominant pair of solutions that determines the cutoff, we evaluate the ATI spectrum within the SPM as

$$\big|T_{\text{res}}^{m,n}(k_f)\big|^2 \sim \left| \sum_{s=\{c+,c-\}} \frac{\exp\big[i S_{k_f}^{m,n}(k_i^s, t_1^s, t_2^s)\big]}{\big[\Delta_{k_f}^{m,n}(k_i^s, t_1^s, t_2^s)\big]^{1/2}} \right|^2, \qquad (37)$$

and simply drop the unphysical solution $\{k_i^{c-}, t_1^{c-}, t_2^{c-}\}$ for energies beyond the cutoff. Although the absolute spectral intensity is lost in Eq. (37), the SPM analysis enables us to find well-defined cutoffs in different ionic channels, and to identify the corresponding rescattering processes.

III. RESULTS AND DISCUSSION

A. Two-electron TDSE versus SAEA

We first investigate the validity of the SAEA for a fixed laser intensity of 8×10^{13} W/cm², but at different wavelengths. Figure 1 shows the ATI spectra in the lowest three ionic
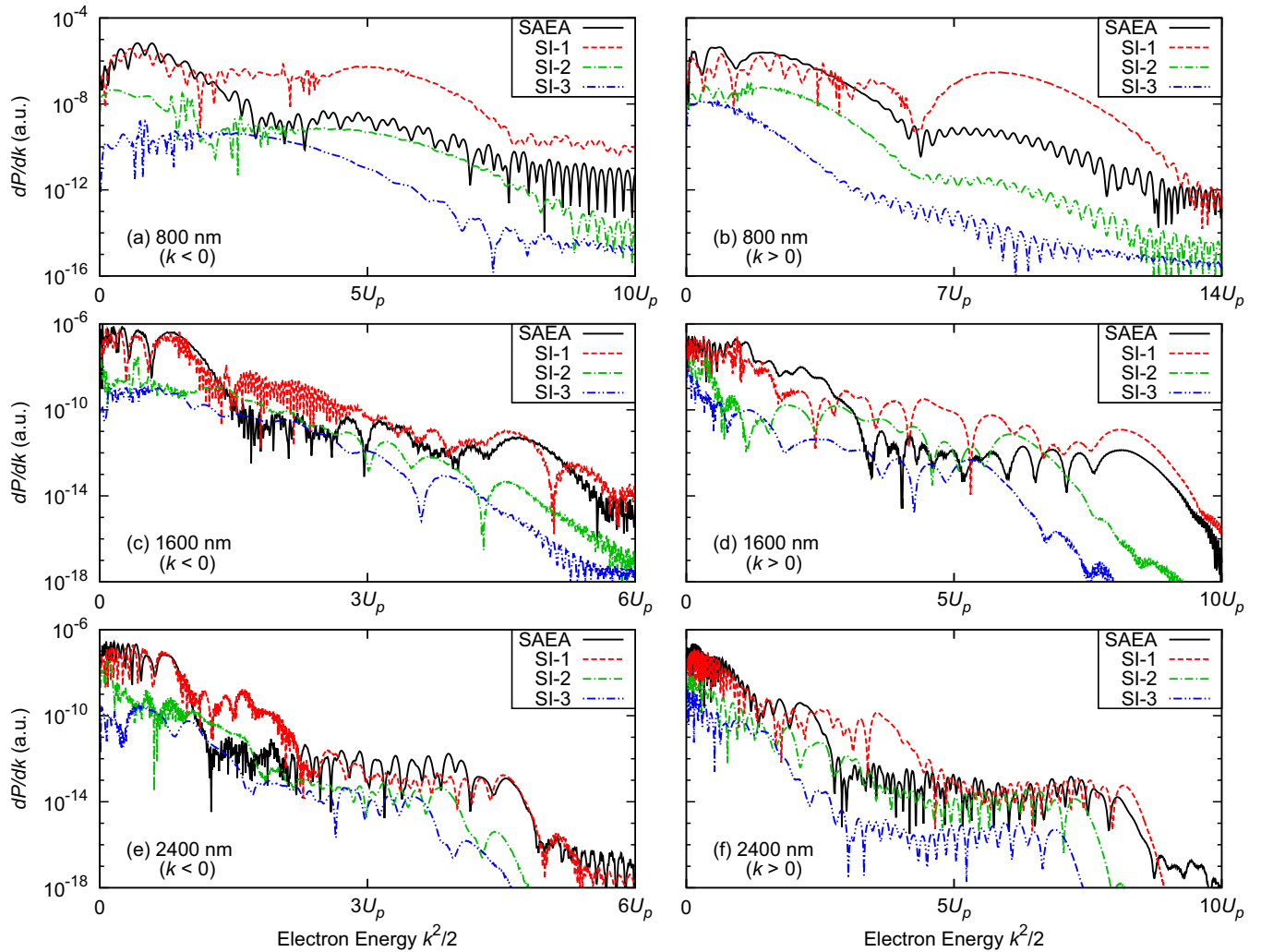
FIG. 1. ATI spectra computed within the SAEA, compared with the SI spectra in the lowest three ionic channels (SI-1, SI-2, and SI-3) extracted from the two-electron TDSE, for two-cycle laser pulses with wavelengths of 800, 1600, and 2400 nm. The peak intensity is fixed at 8×10^{13} W/cm^2.

channels obtained from the two-electron TDSE [Eq. (1)] compared with the ATI spectra obtained from the SAEA TDSE [Eq. (6)], for wavelengths of 800, 1600, and 2400 nm. For the considered two-cycle pulses, there exists obvious asymmetry in the two opposite directions ($k < 0$ and $k > 0$) and the prediction of the typical $10U_p$ cutoff (for long pulses with more than 10 cycles) is not valid.

Figure 1 shows that, in general, the SI in the ground-state ionic channel (SI-1) is dominant while the ATI spectra in the excited-state ionic channels are much weaker. The total SI spectra (not shown) are well represented by the SI-1 spectra. Therefore we focus on the comparison between the SI-1 and SAEA spectra, to study the validity of the SAEA. For the wavelength of 800 nm, it is difficult to clearly identify the ATI plateau and cutoff features. Also in Figs. 1(a) and 1(b) there exists a large disagreement between the SI-1 and SAEA spectra, especially in the high-energy region, where the SI-1 and SAEA spectral intensities differ by around two orders of magnitude. Such disagreement becomes smaller and the plateau and cutoff features become more pronounced, as the wavelength increases to 1600 nm and 2400 nm. For a

wavelength of 2400 nm, the high-energy part of the SAEA spectra is quite similar to that of the SI-1 spectra (and also the total SI spectra). In terms of the high-order ATI spectra corresponding to the back-rescattered electrons, we conclude that the SAEA works better at longer wavelengths for a fixed laser intensity.

A useful quantity for classifying strong-field ionization is the Keldysh parameter $\gamma = \sqrt{I_p/2U_p}$ [10]. For a fixed laser intensity, the ponderomotive energy U_p becomes larger as the wavelength increases, resulting in a smaller Keldysh parameter γ, which means that the ionization dynamics become more tunneling-like. Thus the conclusion drawn from Fig. 1 implies that the SAEA works better for dynamics in the tunneling ionization regime. Now we investigate the validity of the SAEA from a different perspective. We vary the intensity with the wavelength, keeping U_p (and γ) fixed. The ponderomotive energy is fixed at $U_p = 1.58$, which is determined by the laser parameters used in Figs. 1(e) and 1(f). The Keldysh parameter for the 1D model of He is $\gamma = 0.49 < 1$, which is in the tunneling ionization regime. For wavelengths of 800 and 1600 nm, the corresponding intensities are 7.2×10^{14} and
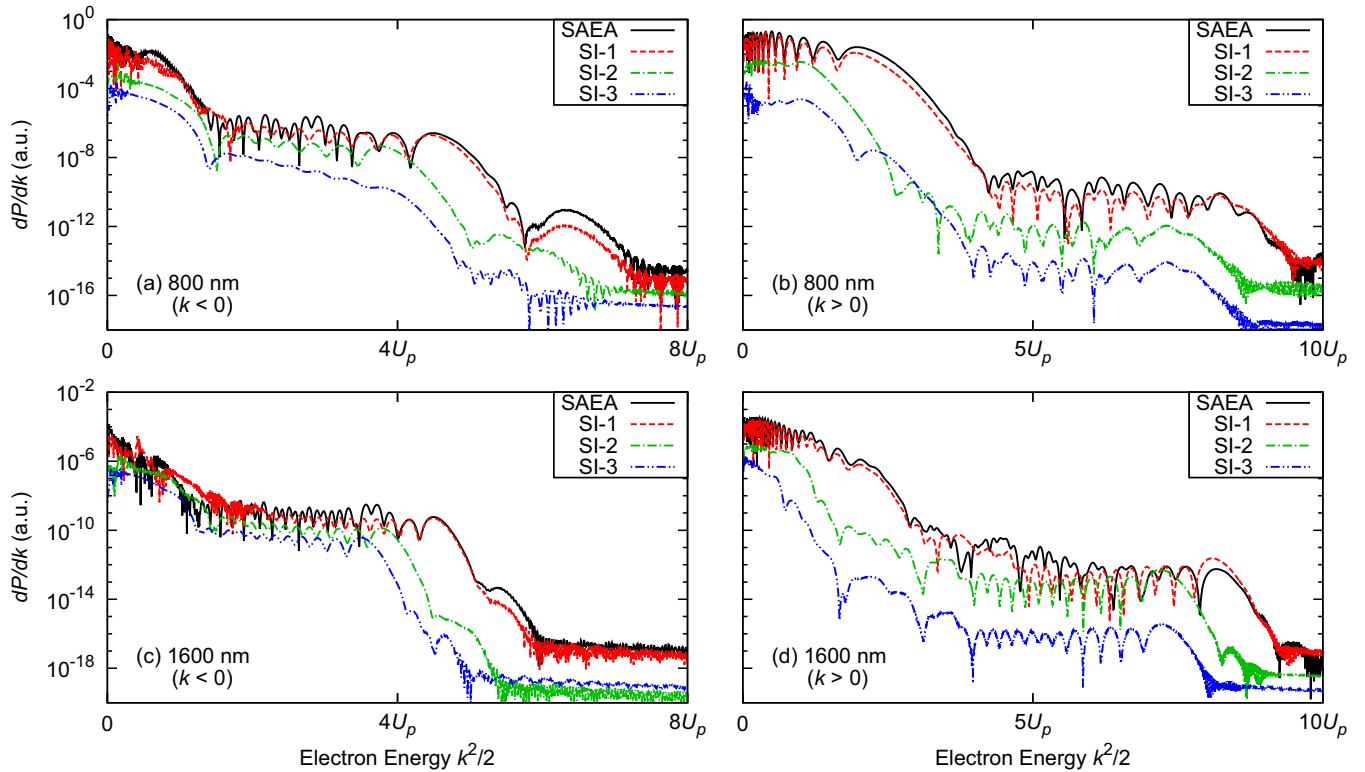
FIG. 2. ATI spectra computed within the SAEA, compared with the SI spectra in the lowest three ionic channels (SI-1, SI-2, and SI-3) extracted from the two-electron TDSE, for two-cycle laser pulses with wavelengths of 800 and 1600 nm. The corresponding peak intensities are 7.2×10^{14} W/cm^2 (for 800 nm) and 1.8×10^{14} W/cm^2 (for 1600 nm), keeping $U_p = 1.58$, as in Figs. 1(e) and 1(f).

1.8×10^{14} W/cm^2, respectively, and the results are presented in Fig. 2. Similarly to Figs. 1(e) and 1(f), Fig. 2 shows good agreement between the SAEA and SI-1 spectra, especially for energies near the cutoff. This means that the SAEA could also be applied to the near-infrared regime (e.g., 800 nm), as long as the ponderomotive energy is large.

The large U_p leads to high-energy rescattering electrons, which can be used for high-resolution imaging of ultrafast dynamics with the LIED technique. Our work indicates that the large U_p also makes the SAEA applicable for the theoretical analysis of the LIED. To achieve large U_p, it is more practical to increase the wavelength than the intensity. The LIED technique based on mid-infrared laser sources has a great advantage that the problematic ionization saturation can be easily avoided for such long wavelengths.

From Figs. 1 and 2, we also find that the SI in different ionic channels have different cutoffs. For example, one can observe in Figs. 1(e) and 1(f) that the cutoff energies for both $(k < 0)$ and $(k > 0)$ decrease in sequence from SI-1 to SI-3. Although the spectral intensities of the SI in the excited-state ionic channels are generally much lower than that of the SI-1, their cutoffs are indeed signatures of two-electron dynamics, which cannot be described within the SAEA. To study two-electron dynamics in the SI of the helium model, we turn to the application of the two-electron SFA described in Sec. II.

B. Two-electron TDSE versus two-electron SFA

As discussed in Sec. II, we consider rescattering processes to analyze the channel-resolved ATI cutoffs via the transition probabilities of Eq. (37). For any final state in a specific ionic channel (n), there are many possible intermediate states in different ionic channels (m). To isolate the dominant rescattering process, we use the fact that the first step, i.e., the SI in the mth channel, is exponentially sensitive to the ionization potential ($E_m - E_g$). Among all the rescattering processes, the first-step SI that goes into the ground-state ionic channel ($m = 1$) is the most probable. Therefore we restrict ourselves to $T_{\text{res}}^{1,n}$ terms in the SFA and find the corresponding cutoffs based on the SPM analysis. In the SPM analysis, we only consider the dominant saddle-point solutions in the high-energy region, which correspond to backward rescattering processes. In the following discussion, we only consider the laser parameters used in Figs. 1(e) and 1(f), i.e., $\lambda = 2400$ nm and $I = 8 \times 10^{13}$ W/cm^2.

In the SPM analysis, the channel-resolved cutoffs are determined by one pair of saddle-point solutions to Eqs. (31)–(33) regarding the elastic and inelastic rescattering processes. To understand the rescattering in the time domain, we first show in Figs. 3(a) and 3(b) the saddle-point solutions of the ionization time t_1 and the rescattering time t_2 used in the evaluation of the elastic rescattering term $T_{\text{res}}^{1,1}$. Note that only the dominant pair of solutions that determines the cutoff is presented here. The real parts of the solutions could be understood as the physical times where the ionization and rescattering occur. By comparing the solutions with the electric field $F(t) = -\partial_t A(t)$, whose variation is also indicated in Figs. 3(a) and 3(b), one finds that the ionization and rescattering events are confined to small regions of time.
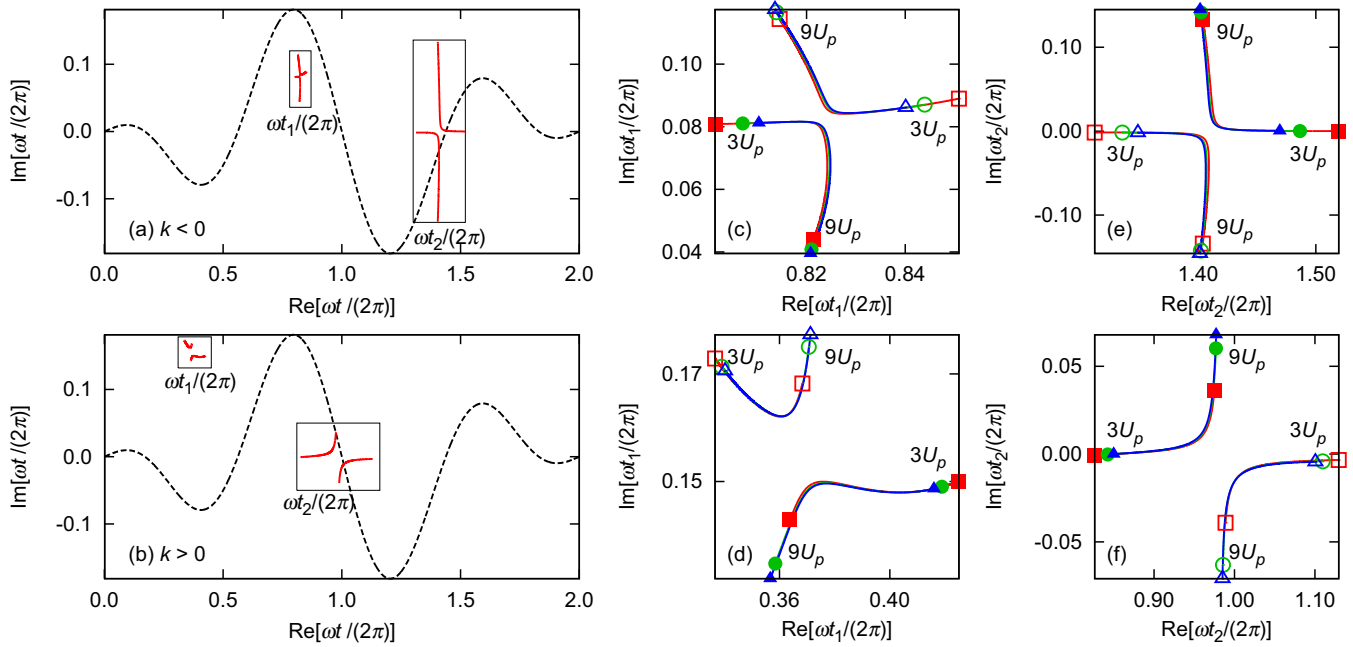
FIG. 3. (a) and (b) Saddle-point solutions of the ionization time t_1 and the rescattering time t_2 (the red solid lines) used to evaluate the elastic rescattering term $T_{\text{res}}^{1,1}$, for the final energy range from $3U_p$ to $9U_p$. The considered laser parameters are the same as in Figs. 1(e) and 1(f). The electric field $F(t) = -\partial_t A(t)$ is presented (in arbitrary units) by the black dashed line. (c)–(f) Zoom-in view of the saddle-point solutions used to evaluate $T_{\text{res}}^{1,1}$ (red lines with square markers), $T_{\text{res}}^{1,2}$ (green lines with circle markers), and $T_{\text{res}}^{1,3}$ (blue lines with triangle markers), for the same final energy range. The line markers indicate the final energies of $3U_p$ and $9U_p$, i.e., the end points of the curves. For energies beyond the cutoff, the solutions labeled by empty markers become unphysical and are dropped in the evaluation of Eq. (37).

To identify the common features of the elastic and inelastic processes and the difference between them, we take a detailed view of the saddle-point solutions for $T_{\text{res}}^{1,1}$, $T_{\text{res}}^{1,2}$, and $T_{\text{res}}^{1,3}$ in Figs. 3(c)–3(f), i.e., for the elastic rescattering in the ground-state ionic channel $T_{\text{res}}^{1,1}$ along with the inelastic rescattering in the excited-state ionic channels $T_{\text{res}}^{1,2}$ and $T_{\text{res}}^{1,3}$. It is observed that the curves of the solutions for different rescattering processes almost coincide. For a specific final energy, however, the solutions for different rescattering processes are different; e.g., the line markers of different types are at different positions. Both the elastic and inelastic rescattering processes considered here have the common feature that the ionization occurs around a peak of the electric field while the rescattering occurs when the electric field is close to zero. It is worth mentioning that the actual ionization dynamics may happen at any time during the laser interaction, which makes the final outcome (e.g., the ATI spectra) complicated to decode. By applying the SPM, however, one can find the dominant processes for explaining parts of the results. Therefore the SPM not only simplifies the evaluation of the integrals in the SFA, but also provides physical insight into the dynamics.

In Fig. 4 we present the SPM analysis of the ATI cutoffs in the lowest three ionic channels. The cutoffs obtained from the SPM analysis are indicated by the dotted vertical lines, and the energies are given in the caption. For the ground-state ionic channel ($n = 1$), the elastic rescattering term $T_{\text{res}}^{1,1}$ gives exact cutoff positions for both the ($k < 0$) and ($k > 0$) cases. The inelastic rescattering terms $T_{\text{res}}^{1,2}$ and $T_{\text{res}}^{1,3}$ give exact cutoff positions for the excited-state ionic channels ($n = 2$) and

($n = 3$), respectively. In terms of the channel-resolved ATI cutoffs, the good agreement between the SPM and the TDSE results implies that the SFA could be a useful qualitative tool for the strong-field ionization in the long-wavelength regime. In the inelastic rescattering, part of the kinetic energy of the freed electron is consumed for the excitation of the ionic state, resulting in a smaller final kinetic energy than that in the elastic rescattering. For the considered 1D model, the energies of the lowest three ionic states are $E_1 = -1.483$, $E_2 = -0.772$, and $E_3 = -0.465$. The energy difference between the ionic ground state and the first excited state is, hence, $E_2 - E_1 = 0.711$. Naively one might expect that this difference should correspond to the difference in the cutoff energies for the SI-1 and SI-2 channels. However, the differences in cutoffs between the SI-1 and SI-2 channels are 1.13 and 1.42 in Figs. 4(a) and 4(b), respectively. In both cases these cutoff differences are very different from the energy difference in the ionic states, and this discrepancy comes from the fact that the vector potential at the rescattering time enters the cutoff analysis [see Eq. (33)]. Similar analysis can be performed for the other cutoffs, and the conclusions are the same.

In closing this section, we briefly mention that although the SFA has been widely applied, it is still a theoretical method under investigation and modification. It is well known that the SFA has drawbacks such as the loss of gauge invariance and the neglect of Coulomb effects, which has stimulated many studies aiming at improving the SFA (see, e.g., recent publications [40–42]). For our purpose of qualitatively determining the channel-resolved ATI cutoffs, the presented two-electron SFA and SPM analyses are demonstrated to be sufficient. To
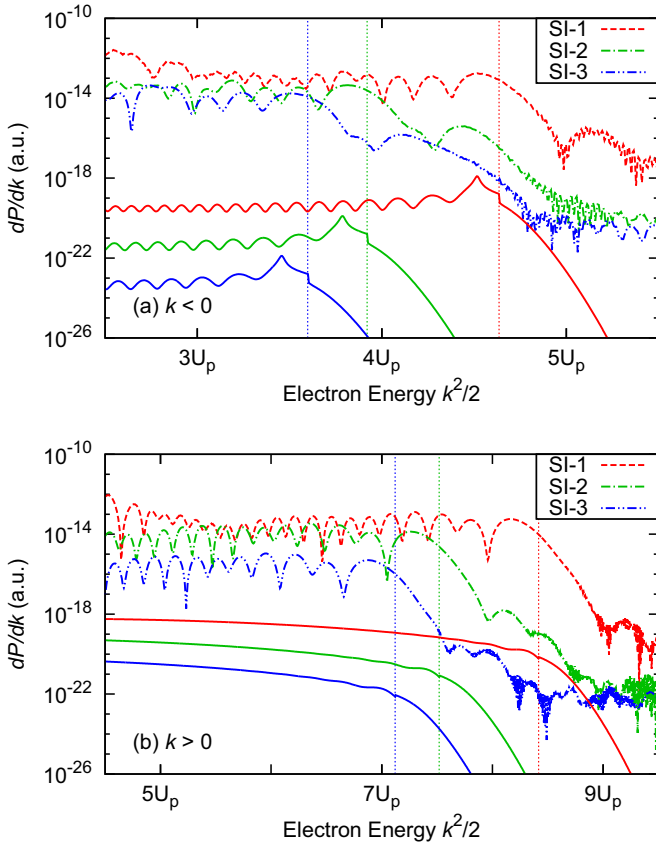
FIG. 4. Channel-resolved ATI cutoffs analyzed with the SFA and the SPM, for the same laser parameters as in Figs. 1(e) and 1(f). The solid lines, from top to bottom, are the channel-resolved high-energy ATI spectra obtained from $T_{\mathrm{res}}^{1,1}$, $T_{\mathrm{res}}^{1,2}$, and $T_{\mathrm{res}}^{1,3}$, respectively. The vertical dotted lines, from right to left, indicate the corresponding cutoffs obtained from the SPM analysis, i.e., the cutoff energies of 7.33, 6.20, 5.69 in (a) and 13.31, 11.89, 11.26 in (b). For better visualization, the solid curves are vertically shifted so that they are clearly separated. The SI spectra in the lowest three ionic channels (SI-1, SI-2, and SI-3) extracted from the two-electron TDSE are also presented for comparison.

understand all the spectral features, however, one needs an improved version of the SFA for multielectron systems.

IV. COCLUSION AND OUTLOOK

We studied the channel-resolved ATI of He in the long-wavelength regime by solving the two-electron TDSE in one dimension, and examined the SAEA and the SFA including rescattering for the two-electron model. For the description of the high-energy rescattered electrons in the ground-state ionic channel, the SAEA was found to perform better with increasing U_p. This finding to some extent validates the SAEA, which is, e.g., commonly used in the theoretical analysis of LIED. The SI in the excited-state ionic channels generally shows much weaker spectral intensity than that in the ground-state ionic channel. The channel-resolved ATI cutoffs are clear signatures of two-electron dynamics, which are beyond the applicability of the SAEA. Regarding the channel-resolved ATI cutoffs at the wavelength of 2400 nm, we investigated the elastic and inelastic rescattering processes by applying the SFA and the SPM, and found good agreement of the cutoff positions between the SPM and the TDSE results. Therefore the two-electron SFA including elastic and inelastic rescattering is proven to be a useful tool for qualitative studies of the strong-field ionization in the long-wavelength regime. Since the full TDSE calculations of multielectron systems are very challenging for long-wavelength laser interactions, it is mandatory to seek good theoretical methods that require fewer computational resources. The two-electron 1D model is a practical reference for developing and examining multielectron theories in the long-wavelength regime.

[1] P. Agostini, F. Fabre, G. Mainfray, G. Petite, and N. K. Rahman, Free-Free Transitions Following Six-Photon Ionization of Xenon Atoms, Phys. Rev. Lett. **42**, 1127 (1979).

[2] J. Eberly, J. Javanainen, and K. Rzążewski, Above-threshold ionization, Phys. Rep. **204**, 331 (1991).

[3] W. Becker, F. Grasbon, R. Kopold, D. B. Milošević, G. Paulus, and H. Walther, Above-threshold ionization: From classical features to quantum effects, Adv. At. Mol. Opt. Phys. **48**, 35 (2002).

[4] D. B. Milošević, G. G. Paulus, D. Bauer, and W. Becker, Above-threshold ionization by few-cycle pulses, J. Phys. B **39**, R203 (2006).

[5] T. Zuo, A. Bandrauk, and P. Corkum, Laser-induced electron diffraction: A new tool for probing ultrafast molecular dynamics, Chem. Phys. Lett. **259**, 313 (1996).

[6] B. Wolter, M. G. Pullen, M. Baudisch, M. Sclafani, M. Hemmer, A. Senftleben, C. D. Schröter, J. Ullrich, R. Moshammer, and J. Biegert, Strong-Field Physics with Mid-IR Fields, Phys. Rev. X **5**, 021034 (2015).

[7] C. I. Blaga, J. Xu, A. D. DiChiara, E. Sistrunk, K. Zhang, P. Agostini, T. A. Miller, L. F. DiMauro, and C. Lin, Imaging ultrafast molecular dynamics with laser-induced electron diffraction, Nature (London) **483**, 194 (2012).

[8] M. G. Pullen, B. Wolter, A.-T. Le, M. Baudisch, M. Hemmer, A. Senftleben, C. D. Schröter, J. Ullrich, R. Moshammer, C.-D. Lin *et al.*, Imaging an aligned polyatomic molecule with laser-induced electron diffraction, Nat. Commun. **6**, 7262 (2015).

[9] B. Wolter, M. G. Pullen, A.-T. Le, M. Baudisch, K. Doblhoff-Dier, A. Senftleben, M. Hemmer, C. D. Schröter, J. Ullrich, T. Pfeifer, R. Moshammer, S. Gräfe, O. Vendrell, C. D. Lin, and J. Biegert, Ultrafast electron diffraction imaging of bond breaking in di-ionized acetylene, Science **354**, 308 (2016).

[10] L. V. Keldysh, Ionization in the field of a strong electromagnetic wave, Zh. Eksp. Teor. Fiz. **47**, 1945 (1964) [Sov. Phys. JETP **20**, 1307 (1965)].

[11] F. H. M. Faisal, Multiple absorption of laser photons by atoms, J. Phys. B **6**, L89 (1973).

[12] H. R. Reiss, Effect of an intense electromagnetic field on a weakly bound system, Phys. Rev. A **22**, 1786 (1980).

[13] R. Kopold, W. Becker, and M. Kleber, Quantum path analysis of high-order above-threshold ionization, Opt. Commun. **179**, 39 (2000).

[14] R. Kopold, W. Becker, H. Rottke, and W. Sandner, Routes to Nonsequential Double Ionization, Phys. Rev. Lett. **85**, 3781 (2000).

[15] C. Figueira de Morisson Faria, H. Schomerus, and W. Becker, High-order above-threshold ionization: The uniform approximation and the effect of the binding potential, Phys. Rev. A **66**, 043413 (2002).

[16] D. B. Milošević and W. Becker, Role of long quantum orbits in high-order harmonic generation, Phys. Rev. A **66**, 063417 (2002).

[17] C. Figueira de Morisson Faria, H. Schomerus, X. Liu, and W. Becker, Electron-electron dynamics in laser-induced nonsequential double ionization, Phys. Rev. A **69**, 043405 (2004).

[18] D. B. Milošević, G. G. Paulus, and W. Becker, Ionization by few-cycle pulses: Tracing the electron orbits, Phys. Rev. A **71**, 061404 (2005).

[19] D. B. Milošević, E. Hasović, M. Busuladžić, A. Gazibegović-Busuladžić, and W. Becker, Intensity-dependent enhancements in high-order above-threshold ionization, Phys. Rev. A **76**, 053410 (2007).

[20] D. Dimitrovski, C. P. J. Martiny, and L. B. Madsen, Strong-field ionization of polar molecules: Stark-shift-corrected strong-field approximation, Phys. Rev. A **82**, 053404 (2010).

[21] T.-M. Yan, S. V. Popruzhenko, M. J. J. Vrakking, and D. Bauer, Low-Energy Structures in Strong Field Ionization Revealed by Quantum Orbits, Phys. Rev. Lett. **105**, 253002 (2010).

[22] T. Shaaran, M. T. Nygren, and C. Figueira de Morisson Faria, Laser-induced nonsequential double ionization at and above the recollision-excitation-tunneling threshold, Phys. Rev. A **81**, 063413 (2010).

[23] T. Shaaran, C. Figueira de Morisson Faria, and H. Schomerus, Causality and quantum interference in time-delayed laser-induced nonsequential double ionization, Phys. Rev. A **85**, 023423 (2012).

[24] A. S. Maxwell and C. Figueira de Morisson Faria, Quantum interference in time-delayed nonsequential double ionization, Phys. Rev. A **92**, 023421 (2015).

[25] A. S. Maxwell and C. Figueira de Morisson Faria, Controlling Below-Threshold Nonsequential Double Ionization via Quantum Interference, Phys. Rev. Lett. **116**, 143001 (2016).

[26] R. Grobe and J. H. Eberly, Photoelectron Spectra for a Two-Electron System in a Strong Laser Field, Phys. Rev. Lett. **68**, 2905 (1992).

[27] M. Lein, E. K. U. Gross, and V. Engel, Intense-Field Double Ionization of Helium: Identifying the Mechanism, Phys. Rev. Lett. **85**, 4707 (2000).

[28] M. Ruggenthaler and D. Bauer, Rabi Oscillations and Few-Level Approximations in Time-Dependent Density Functional Theory, Phys. Rev. Lett. **102**, 233001 (2009).

[29] T. N. Rescigno and C. W. McCurdy, Numerical grid methods for quantum-mechanical scattering problems, Phys. Rev. A **62**, 032706 (2000).

[30] A. Scrinzi, Infinite-range exterior complex scaling as a perfect absorber in time-dependent problems, Phys. Rev. A **81**, 053845 (2010).

[31] M. Weinmüller, M. Weinmüller, J. Rohland, and A. Scrinzi, Perfect absorption in Schrödinger-like problems using non-equidistant complex grids, J. Comput. Phys. **333**, 199 (2017).

[32] T. J. Park and J. C. Light, Unitary quantum time evolution by iterative Lanczos reduction, J. Chem. Phys. **85**, 5870 (1986).

[33] X. Guan, O. Zatsarinny, K. Bartschat, B. I. Schneider, J. Feist, and C. J. Noble, General approach to few-cycle intense laser interactions with complex atoms, Phys. Rev. A **76**, 053411 (2007).

[34] R. Kosloff and H. Tal-Ezer, A direct relaxation method for calculating eigenfunctions and eigenvalues of the Schrödinger equation on a grid, Chem. Phys. Lett. **127**, 223 (1986).

[35] L. Tao and A. Scrinzi, Photo-electron momentum spectra from minimal volumes: The time-dependent surface flux method, New J. Phys. **14**, 013021 (2012).

[36] A. Scrinzi, *t*-SURFF: Fully differential two-electron photo-emission spectra, New J. Phys. **14**, 085008 (2012).

[37] A. Zielinski, V. P. Majety, and A. Scrinzi, Double photo-electron momentum spectra of helium at infrared wavelength, Phys. Rev. A **93**, 023406 (2016).

[38] L. A. A. Nikolopoulos, T. K. Kjeldsen, and L. B. Madsen, Three-dimensional time-dependent Hartree-Fock approach for arbitrarily oriented molecular hydrogen in strong electromagnetic fields, Phys. Rev. A **76**, 033402 (2007).

[39] A. Becker and F. H. M. Faisal, Intense-field many-body *S*-matrix theory, J. Phys. B **38**, R1 (2005).

[40] A. Galstyan, O. Chuluunbaatar, A. Hamido, Y. V. Popov, F. Mota-Furtado, P. F. O'Mahony, N. Janssens, F. Catoire, and B. Piraux, Reformulation of the strong-field approximation for light-matter interactions, Phys. Rev. A **93**, 023422 (2016).

[41] F. H. M. Faisal, Strong-field *S*-matrix theory with final-state Coulomb interaction in all orders, Phys. Rev. A **94**, 031401 (2016).

[42] M. Klaiber, J. Daněk, E. Yakaboylu, K. Z. Hatsagortsyan, and C. H. Keitel, Strong-field ionization via a high-order Coulomb-corrected strong-field approximation, Phys. Rev. A **95**, 023403 (2017).